Structural environment influence on Faraday Effect in Tb 3+ and Pr 3+ co-doped Fluorophosphate Glass and Glass-ceramics containing TbOF nanocrystals

Brice Bellanger, Wagner Correr, Emmanuel Véron, Cécile Genevois, Yannick Ledemi, Mathieu Allix, Younès Messaddeq

Structural environment influence on Faraday Effect in Tb^{3+} and Pr^{3+} co-doped Fluorophosphate Glass and Glass-ceramics containing TbOF nanocrystals

Brice Bellanger,[*a] Wagner Correr,[a] Emmanuel Véron,[b] Cécile Genevois,[b] Yannick Ledemi,[a] Mathieu Allix[b] and Younès Messaddeq[a]

[a] Center of Optics, Photonics and Lasers, Laval University, Québec, Qc, Canada

[b] Conditions Extrêmes et Matériaux: Haute Température et Irradiation, CEMHTI-CNRS UPR3079, 1D avenue de la Recherche Scientifique, 45071, Orléans Cedex 2, France

TOC

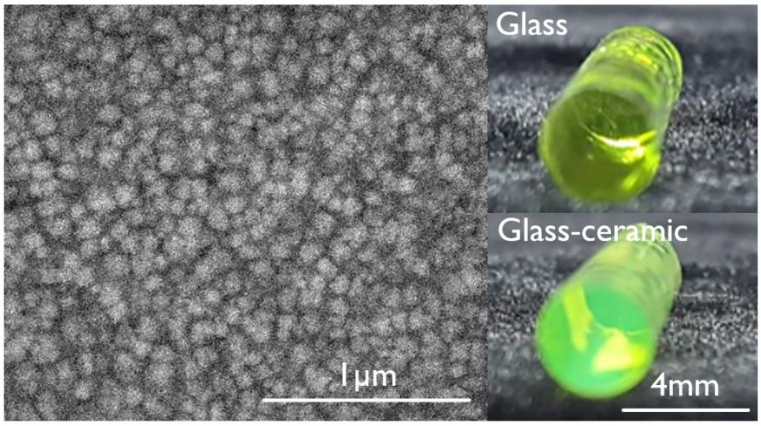

Abstract

The influence of structural environment of lanthanide ions on the co-doping Faraday effect is explored within fluorophosphate glasses and glass ceramics. In a first part, the crystallization process of a glass with a nominal composition 35 $NaPO_3$ – 15 BaF_2 – 50 TbF_3 is explored in function of duration and temperature of the ceramization process. X-ray diffraction analysis and STEM-HAADF allowed the identification of crystalline TbOF cubic fluorite phase in these glass-ceramics, with a maximum crystalline fraction of 44 wt.% for a crystallite size of 46 nm for the sample heat-treated 10h at 394°C. In a second part, TbOF glass-ceramics following the composition law 35 $NaPO_3$ – 15 BaF_2 – 0.5 ((100-x) TbF_3 – x PrF_3) with x = 0, 1, 2, 3, 4 and 5 are prepared at the optimal heat treatment of 10h at 394°C corresponding to maximal crystalline fraction and optical transmission. The Verdet constants of these co-doped glass-ceramics are characterized and compared to the ones of the parent glasses. The maximum co-doping efficiency reaches 1.075 for the glass-ceramic, compared to a value of 1.037 for the

corresponding co-doped glass samples. The structural organization around the lanthanide cation site increases the co-doping influence on the Faraday Effect by optimization of the superexchange interaction.

Introduction

The Faraday effect (FE) consists in the rotation of polarization of the light across a magneto-optically sensitive medium submitted to an external magnetic field. This effect is of strong interest for optical isolators in telecommunication and high-power laser fields[1]. The Verdet constant is used to characterize this phenomenon considering the size of the magneto-optical material, the angle of rotation and the value of the magnetic field applied. The higher this Verdet constant is in absolute values, the higher the FE is. From visible to near infrared ranges, lanthanide ions are the most efficient paramagnetic elements to use. In the lanthanide family, terbium +III is the most efficient ion in reason of its transition $4f^8 \rightarrow 4f^7$ 5d, and its strong magnetic susceptibility (J = 6, g = 1.46) [2,3].

The Faraday material mostly used commercially is a garnet single crystal composed of terbium and gallium oxides named TGG ($Tb_3Ga_5O_{12}$) which shows a Verdet constant of -134 $rad.T^{-1}.m^{-1}$ at 632 nm.[4] Some oxide glasses mainly based on silicate and germanate glass matrix have been studied with a maximal Verdet constant reported of -168.6 $rad.T^{-1}.m^{-1}$ at 632 nm for a borogermanate glass with 45 mol.% of Tb_2O_3 [3,5–10]. In our recent work on fluorophosphate glasses, a glass of composition 35 $NaPO_3$ – 15 BaF_2 – 50 TbF_3 has been successfully incorporated in the network without observing any devitrification, with a maximal Verdet constant measured for this glass of -80 $rad.T^{-1}.m^{-1}$ at 632 nm [11]. To go beyond these limits, substituting a small part of terbium by another lanthanide ion might be a promising avenue. Indeed, an increase of variable amplitude

according to the selected lanthanide has been recently demonstrated in TGG single crystals by partly substituting Tb^{3+} with Nd^{3+}, Er^{3+}, Tm^{3+}, Dy^{3+}, Ce^{3+}, Pr^{3+} or Ho^{3+} comparing to pure TGG single crystals. Among these lanthanide ions, the weakest effect is observed by co-doping with Nd^{3+} and Er^{3+} ions with an increasing Verdet constant of -145 and -145.3 $rad.T^{-1}.m^{-1}$ at 632 nm, respectively [12,13]. An intermediate increase of the Verdet constant is then reported for Ce^{3+}, Dy^{3+}, Tm^{3+} and Pr^{3+} substitution in TGG single crystal with a Verdet constant of -157.3, -178.6, -178.6 and -200.1 $rad.T^{-1}.m^{-1}$ at 632 nm, respectively [14–17]. The strongest amelioration of Verdet constant via co-doping is reported for Ho^{3+} substitution with a Verdet constant of -214.9 $rad.T^{-1}.m^{-1}$ at 632 nm [18]. This phenomenon is still not well understood. The attribution to superexchange interaction between two cationic sites of different nature is the most accepted explanation to date, but further investigation is required [12–18].

Recently, in our research group, the observation of this effect for three lanthanide cations Pr^{3+}, Ho^{3+} and Dy^{3+} co-doped terbium fluorophosphate glasses has been reported [19]. The control of all the parameters of influence on the Faraday Effect as the temperature, the sample thickness, the magnetic field, the wavelength of measurement and the ionic density were taken into account to validate the co-doping origin of this Verdet constant increase. The Tb^{3+} single-doped glass sample shows a Verdet constant of -81.9 $rad.T^{-1}.m^{-1}$ at 600 nm while Pr^{3+}, Ho^{3+} and Dy^{3+} co-doped glass sample exhibit respectively a Verdet constant of -84.2, -84.5 and -84.5 $rad.T^{-1}.m^{-1}$ at 600 nm. However, the increase observed seems to be lower in glassy materials compared to single crystal.

To help understanding the origin of this phenomenon, which is closely related to the lanthanide cation local environment and inter-cationic distances, the controlled

crystallization of co-doped glasses of appropriate compositions could provide useful information. Indeed, previous studies carried out on rare-earth co- or triply- doped transparent oxyfluoride (including fluorophosphate) glass-ceramics have evidenced the influence of heat-treatment on the distribution of rare-earth ions and their integration within the nanocrystalline phase [20–26].

In the first part of this work, the crystallization process of fluorophosphate glasses singly doped with terbium of composition law 35 $NaPO_3$ – 15 BaF_2 – 50 TbF_3 is investigated. For an additional comprehension of co-doping effect, as the main difference between glass and single crystal is related to the local environment of cations, the controlled crystallization of these materials could provide crucial information. The fine control of the crystallization process is a key point to reach a maximal crystalline fraction and a minimal impact on the optical material transparency, which are the two most important parameters to monitor the structural modification of lanthanide environment and measuring the Faraday Effect, respectively. This crystallization process will be investigated by thermal, optical, structural and morphological analyses. In a second part, fluorophosphate glass-ceramics elaborated from glass with the following composition law 35 $NaPO_3$ – 15 BaF_2 – 0.5 ((100-x) TbF_3 – x PrF_3) with x = 0, 1, 2, 3, 4 and 5 are investigated. The influence of praseodymium on the crystallization process and the final properties of the glass-ceramics is discussed. Then, the magneto-optical properties of glass and glass-ceramics from same composition are compared.

Experimental

The glass samples were prepared by conventional melt-quenching method following the composition law: 35 $NaPO_3$ – 15 BaF_2 – 0.5 ((100-x) TbF_3 – x PrF_3) with x = 0, 1, 2, 3, 4, 5. They were elaborated from precursors of sodium metaphosphate, barium fluoride, terbium fluoride and praseodymium fluoride. Mixtures of 10 g with appropriate proportions of powder precursors were melted at 1100°C for 30 minutes in a Pt/Rh crucible. A Pt lid was used to limit the evaporation of the glass components . The melts were then poured into a stainless-steel mold preheated at 330°C and annealed for a duration of 6 hours and slowly cooled down to room temperature. Homogeneous and bubble-free glass rods of 4 mm in diameter and 5 cm in length were obtained, with a colour varying from colorless to greenish as a function of the praseodymium content.

The glass-ceramic samples were then prepared from the terbium and terbium-praseodymium co-doped fluorophosphate parent glasses by thermal treatment above their respective glass transition temperature, at different temperatures ranging from 379°C to 439°C, in a Naberthem muffle furnace for different durations up to 30 hours. Ceramization conditions (*i.e.*, temperature and duration) were first explored on terbium fluorophosphate parent glasses to obtain glass-ceramics of desired optical transparency with reproducibility. The as-defined optimal ceramization conditions were then employed to produce the transparent praseodymium-terbium co-doped fluorophosphate glass-ceramics and compare their magneto-optical properties.

For structural analysis, pieces of glass rod were ground to perform X-ray powder diffraction (XRPD) with an Aeris benchtop X-ray diffractometer from Panalytical with a copper radiation (Cu $K\alpha_{1,2}$ = 1.5432 Å). *In situ* High Temperature Powder XRD patterns

were collected using a conventional θ-θ Bragg–Brentano configuration (Ni-filtered CuK$\alpha_{1,2}$ radiation) on a Bruker-AXS D8 Advance diffractometer fitted with a linear Vantec-1 detector. The diffractometer is equipped with an Anton Paar oven chamber (model HTK 1200 N) able to reach temperatures up to 1200°C. Diagrams were recorded from 15 to 90° (2θ) using a step size of 0.024° and a time by step of 0.5s. The Rietveld method was used to quantify the amorphous phase and consequently the crystalline fraction in glass ceramic sample by using an internal standard with a well-known weight percentage [27,28]. The standard used is a $Tb_{11}O_{20}$ crystalline phase mixed with the samples in a mass ratio of 3:1 during 30 minutes in agate mortar and ethanol. The choice of this standard is based on its absorption close to that of the crystalline phase identified in the glass-ceramic samples and very few diffraction peaks overlapping. Considering the low X-ray micro-absorption contrast (product of linear absorption and particles sizes of all the phases in the sample), Brindley correction [29] was not applied. The X-ray powder diffraction pattern was collected from 17° to 125° in 2θ with a 0.012° step size. Quantification via Rietveld refinement was performed using the TOPAS software using a fundamental approach for the line profile [30].

Scanning electron microscopy (SEM) was performed on fractured pieces of sample with a field emission gun microscope Quanta-3D-FEG (FEI). Scanning transmission electron microscopy – high angle annular dark field (STEM-HAADF) imaging and STEM-EDS elemental mapping were carried out on an ARM200F double corrected microscope (JEOL Ltd) operating at 80kV and fitted with a JEOL SDD CENTURIO EDS system. The differential scanning calorimetry (DSC) diagrams were recorded in aluminium pans on a Netzsch DSC 404 F3 Pegasus at a heating rate of 10°C.min^{-1}. For optical

characterization, the glass rods were cut and polished to obtain samples with two parallel faces of approximately 10x4x2 mm^3 dimensions. The UV-Vis-NIR transmission spectra were recorded in the wavelength range from 1.5 to 10 µm with a Perkin Elmer Frontier FTIR spectrometer, and from 200 to 2000 nm with an Agilent Cary 5000 spectrometer. Electron probe micro-analyses (EPMA) were carried out on as-prepared samples with a SX-100 probe from CAMECA with measurements performed on eight different points to provide an average atomic content for each element.

Regarding Verdet constant measurements, rods of approximately 2 cm of length for 4 mm of diameter with both polished parallel ends were used. To ensure that the two opposite faces are parallel one to each other and perpendicular to the rod longitudinal axis, an Ultrapol ultratec polisher was used to allow fine control of the polishing angle. An automatic experimental setup is used to measure the Verdet constant from 600 to 1100 nm with a high accuracy of 0.01° equivalent to a value of 0.02 $rad.T^{-1}.m^{-1}$ in these experimental conditions [19]. It is constituted of a supercontinuum laser source NKT superK compact, operating from 450 to 2400 nm, used as light source, and coupled to a Brucker monochromator for wavelength selection. A Thorlabs optical chopper operating at 1000 Hz coupled to a Standford Research System model SR830 DSP lock-in amplifier was used to increase the sensitivity. A permanent Nd-based magnet with a magnetic field value of 0.42 Tesla (verified by using a Sypris 5170 magnetic probe) was placed between the polarizer and the analyzer. A Si photodetector PDA36A was used in conjunction with the lock-in coupled to a software for an automatic acquisition of power as a function of the rotation of the analyzer at each wavelength selected for measurement, ensuring high accuracy of the acquisitions.

Results and discussion

Section 1: Terbium fluorophosphate glass-ceramics

An explorative crystallization study has been carried out on 35 $NaPO_3$ – 15 BaF_2 – 50 TbF_3 glass pieces while varying heat-treatment temperatures and durations. The optimum parameters were determined to achieve the maximal crystalline fraction while maintaining an excellent optical transmission close to 80% in the visible and near infrared ranges (for a sample thickness of 2 mm). First, ceramization temperatures ranging from 379°C to 439°C, which correspond to Tg +60°C, were explored for a constant duration of heat treatment, established at 10 hours. Then, ceramization durations ranging from 0 to 30 hours were conducted for a constant temperature of 394°C corresponding to the optimal temperature based on the temperature evolution study. For each sample, the evolution of thermal, structural, optical and morphological properties was performed by DSC, UV-Visible-IR transmission, XRD and SEM imaging respectively.

In situ X-ray diffraction

To gain global knowledge on the crystallization behavior of the glass, *in situ* X-ray Powder diffraction was performed from room temperature up to 600°C. The evolution of the diffraction patterns vs. temperature are shown in figure 1. From room temperature up to 390°C (section A), no crystalline peaks are observed on diffractograms, corresponding to the glass signature. From 390 to 440°C (section B), a crystalline phase with cubic fluorite structure of space group $Fm\bar{3}m$ and a lattice parameter of 5.70Å appears. Then, in the temperature range from 440 to 460°C (section C), similar fluorite structure phase

with a smaller lattice parameter grows preferentially at the expense of the first one, up to a lattice parameter of 5.49Å at 600°C. It can be attributed to a change thermally induced in composition of the fluorite phase as diffusion of atoms out of the crystalline phase. The glass matrix starts to crystallize at 460°C with the formation of $Na_2TbPO_4F_2$ (jcpdf 50-0065) and $BaTb_3F_{17}$ (isostructural to $BaYb_3F_{17}$ jcpdf 85-1150) in section D. $NaTbFPO_4$ (isostructural to $NaDyFPO_4$ jcpdf 53-0183) and $Ba_4Tb_3Na_3F_2(PO_4)_6$ (isostructural to $Ba_4Nd_3Na_3F_2(PO_4)_6$ jcpdf 71-1318) crystalline phases are observed in section E and F respectively.

From this analysis, it appears possible to synthesise glass-ceramics with a single crystalline phase using a thermal treatment temperature between the glass transition temperature and 435°C.

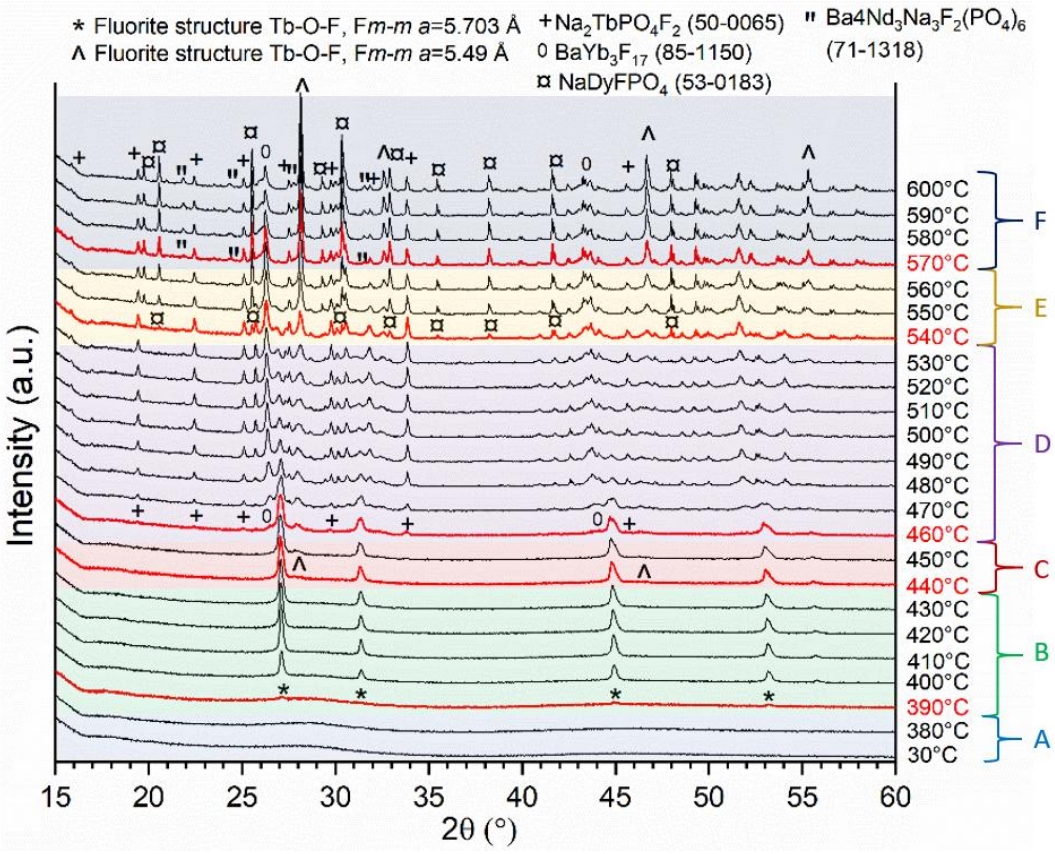

Figure 1 In situ powder X-ray diffraction patterns recorded during heating of a non-doped 35 $NaPO_3$ – 15 BaF_2 – 50 TbF_3 glass from 30 to 600°C.

Transmission electron microscopy and Energy dispersive X-ray Spectroscopy

Scanning transmission electron microscopy - high-angle annular dark-field (STEM-HAADF) imaging conjugated to Energy dispersive X-ray Spectroscopy (EDS) was used to determine the elemental composition of the fluorite structure. The TEM image shown in figure 2 enables the identification of the crystals and amorphous area. Crystals appear darker due to their higher density diffracting the electron beam. STEM-HAADF micrographs and EDS analyses are shown in figure 2. From STEM-HAADF imaging, the chemical contrast shows the presence of heavy elements (bright contrast) in the particles. Indeed, the contrast is related to the average atomic number of the phase, heavier it is, the brighter it appears. From EDS mapping and spot measurements, fluorine appears to be present only in the crystalline phase while oxygen is found both in the glass matrix and in the crystals. It permits to conclude on the formation of oxyfluoride crystals. Concerning cations, phosphorus is present essentially in the glass matrix. Terbium is preferentially located in the crystalline phase although also observable in the glass matrix. Finally, barium does not show specific localisation in the glass-ceramic. According to TEM and XRD results, the composition of the fluorite structure crystalline phase can be attributed to the TbOF cubic phase ($Fm\bar{3}m$ space group) with a possible partial incorporation of barium ion in the structure. The presence of barium in the structure could explain the formation of the second fluorite phase observed by XRPD. Indeed, due to the larger atomic radii of barium (253 pm) in comparison with terbium (225 pm), the formation of a

$Tb_{1-x}Ba_xO_{1-x}F_{1+x}$ material could explain the presence of the second fluorite phase with a decreasing cell parameter due to the diffusion of barium out of the particles.

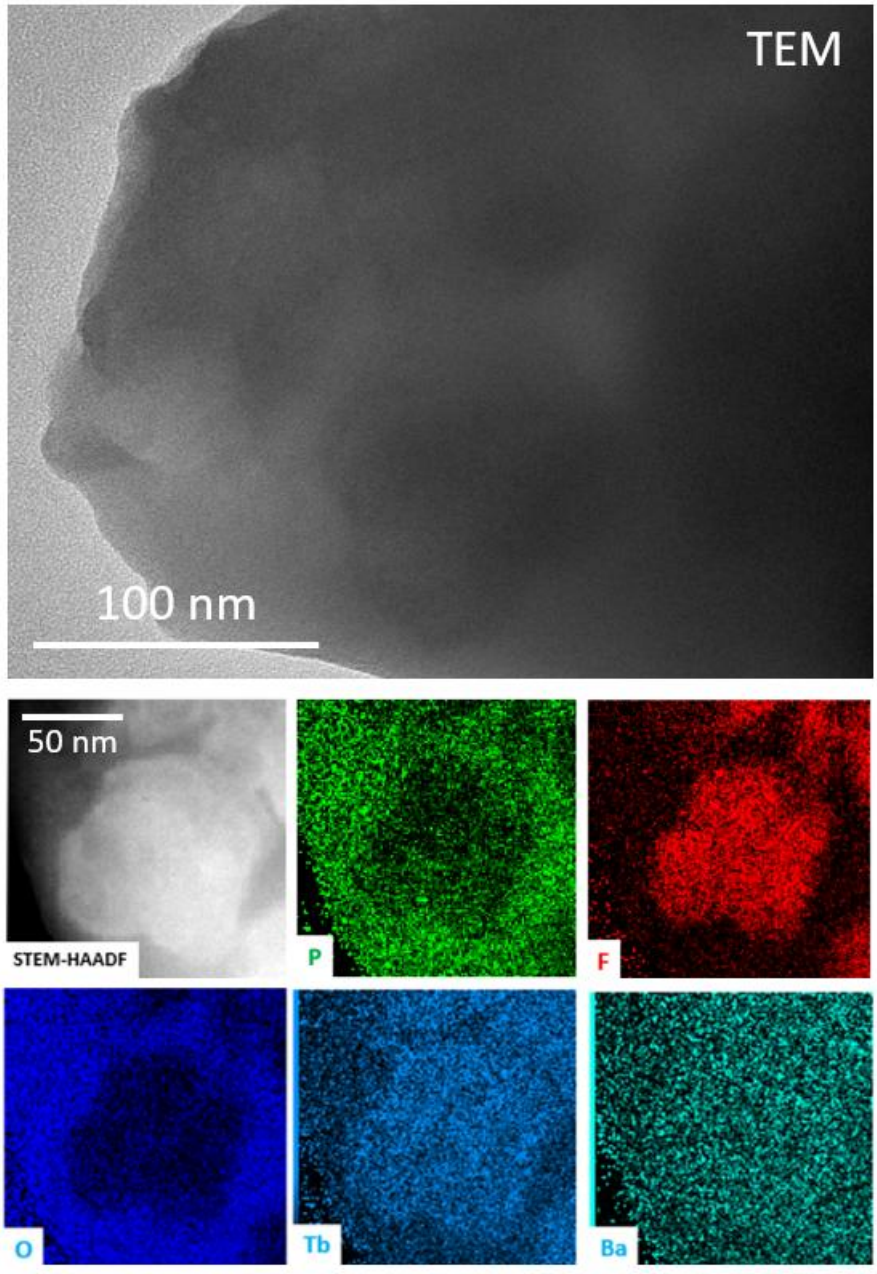

Figure 2. TEM image and Scanning transmission electron microscopy - High-angle annular dark-field (STEM-HAADF) image and EDS maps of undoped glass-ceramic obtained from a heat treatment of 10h at 424°C.

Thermal analysis

The impact of the ceramization temperature on DSC curves is reported in figure 3.a. From theses curves, the glass transition temperature and integrated area below the first peak of crystallization for each temperature are extracted and plotted as a function of ceramization temperature in figure 3.b. The ceramization temperature did not exceed 440°C to only crystallized the first fluorite phase, based on XRPD data. It can be observed that Tg increases with the increasing of the ceramization temperature whereas the integrated area below the first peak of crystallization decreases when the ceramization temperature increases. The glass transition temperature increases non-monotonously from the parent glass (Tg = 372°C) up to a plateau at around Tg = 416°C for the glass-ceramics heat-treated 10h at 424°C and higher. At the same time, the integrated area of the crystallization peak, corrected by the mass used for the measurement, decreases from a plateau at approximately 36 $J.g^{-1}$ down to a value close to zero for ceramization treatments of 10 h at 408°C and higher temperatures. The variation of the glass transition temperature is attributed to the change of composition of the vitreous matrix accordingly with the apparition of a fluorite crystalline phase. Indeed, the crystalline phase "consumes" fluorine from the glassy network, such increasing the reticulation of the glass matrix by switching from oxyfluoride to oxide composition. The variation of the integrated area of the crystallization peak is directly linked to the crystallization process. It is then possible to follow the quantity of crystalline phase remaining at each ceramization temperature and to extrapolate that for a ceramization temperature higher than 394°C no more crystalline phase is produced.

Figure 3.c shows the DSC curves recorded on the Tb-Pr 0% parent glass and $Tb_{1-x}Ba_xO_{1-x}F_{1+x}$ glass-ceramics obtained after thermal treatment at 394 °C for different durations. An increase of the glass transition temperature and a decrease of the area of the first peak of crystallization are observed with increasing the duration of ceramization. The characteristic values extracted from these DSC curves are plotted in figure 3.d as a function of heat-treatment duration. Here, the glass transition temperature increases quite monotonously from 372°C for the parent glass to a plateau around 403°C for the glass-ceramics heat-treated at 394°C for 10h and longer durations. The integrated area of the first peak of crystallization decreases from 36 $J.g^{-1}$ to a value under 5 $J.g^{-1}$ after 10h of heat treatment. These characteristic values follow an exponential function related to the kinetics of crystallization of the crystalline phase. It appears that over 10 hours of heat treatment, no substantial variation of these parameters is observed. The crystallization process reaches a maximum and no more crystalline phase is produced.

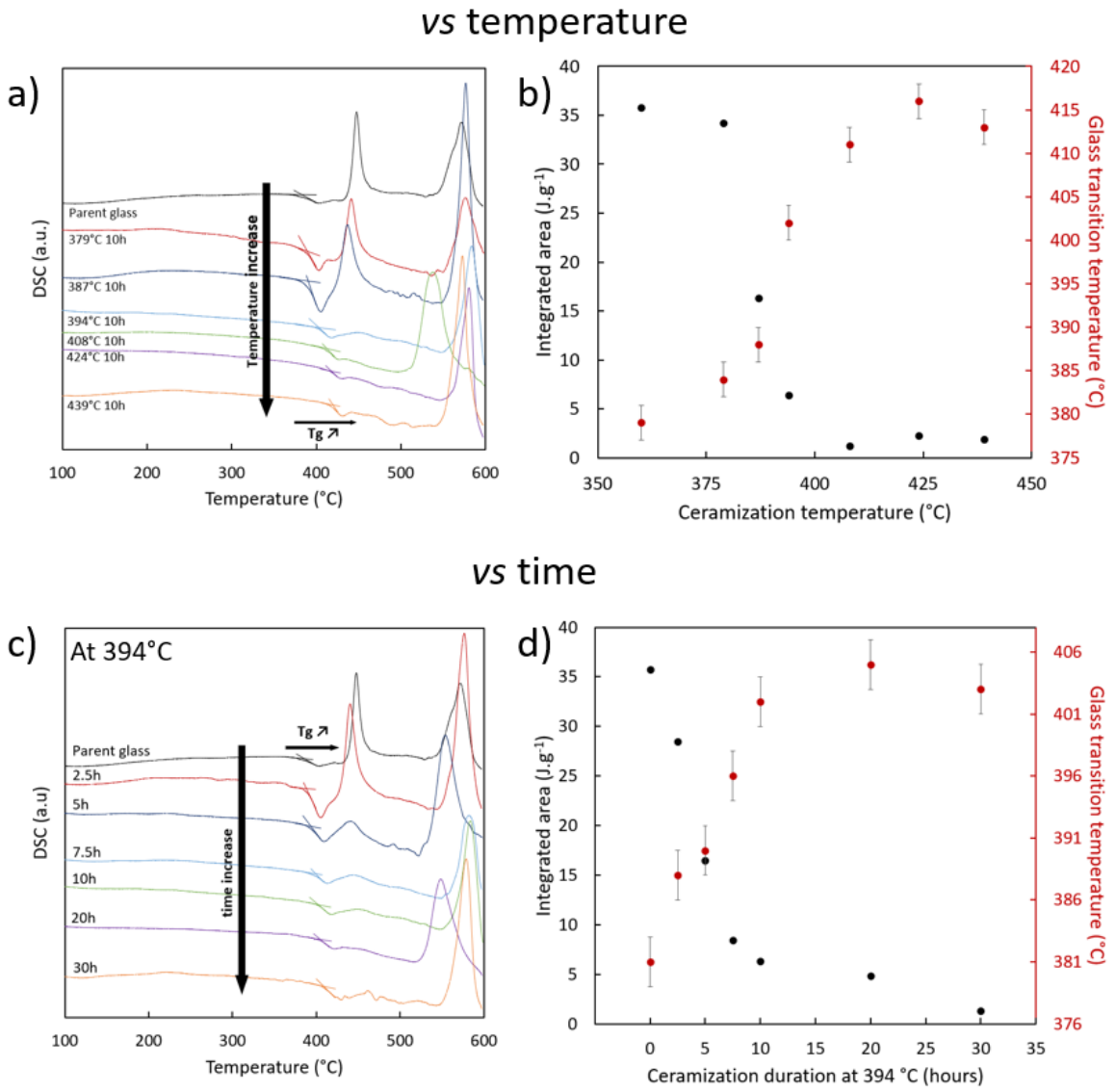

Figure 3. a) DSC curves of Tb-Pr 0% parent glass and heat-treated glass-ceramics for 10h as a function of heat-treatment temperature. The DSC traces were vertically shifted to ease reading. **b)** Glass transition temperature and integrated area below the first peak of crystallization as a function of temperature of ceramization. **c)** DSC curves of Tb-Pr 0% for various time of ceramization treatment from zero to 30 hours for a constant temperature of 394°C. d**)** Vitreous transition temperature and integrated area of the first peak of crystallization in function of time of ceramization.

Structural analysis

X-ray powder diffractograms measured after ceramization treatments of 10 hours at temperatures ranging from room temperature to 439°C are reported in figure 4.a. A single crystalline phase is observed from 387°C to 439°C. It corresponds to the Ba-enrich TbOF cubic fluoride phase (space group $Fm\bar{3}m$) as discussed previously.

The evolution of the crystalline fraction as a function of the ceramization temperature is reported in figure 4.b. The quantification of the amorphous phase and consequently the crystalline fraction were determined by Rietveld refinement using an internal standard method. An increase of the crystalline fraction from zero to values varying from 26 ±2 to 44 ±2 wt.% of crystalline fraction from 394°C is observed. An intermediate point corresponding to 6 ±2 wt.% of crystalline fraction is obtained at 387°C. The crystalline phase is fully formed between 379°C and 394°C for a ceramization time of 10 hours. Above 394°C, the crystalline fraction varies around a mean value of 36 wt.%. These variations can be explained by the existence of surface crystallization. Indeed, the parent glass rod samples have a composition close to the crystallization process during the elaboration [11]. Surface crystallization (white areas) can appear in well defined areas of the final glass parent rod. These sections are discriminated during the preparation of glass-ceramic samples. Nevertheless, the variation of the size of the glass cylinder for ceramization treatment induces a variation of the surface/volume ratio which could induce variation on the determination of the crystalline fraction in the case of residual surface crystallization.

The structural analysis as a function of the duration of the ceramization treatment is illustrated by the diffractograms reported in figure 4.c. It is observed that from 2.5 hours

of heat treatment at 394°C a crystalline phase is formed. The same crystalline phase is observed from 2.5 to 30 hours, which correspond to the same TbOF phase observed in the study in function of temperature. The crystalline fraction determined from XRD experiments shown in figure 4.d increases from zero, corresponding to the amorphous material at t = 0, to a plateau varying from 31 ±3 to 42 ±2 wt.% from 10 hours of heat treatment. The minimum time of ceramization treatment to observe the maximum of crystalline fraction is 10 hours.

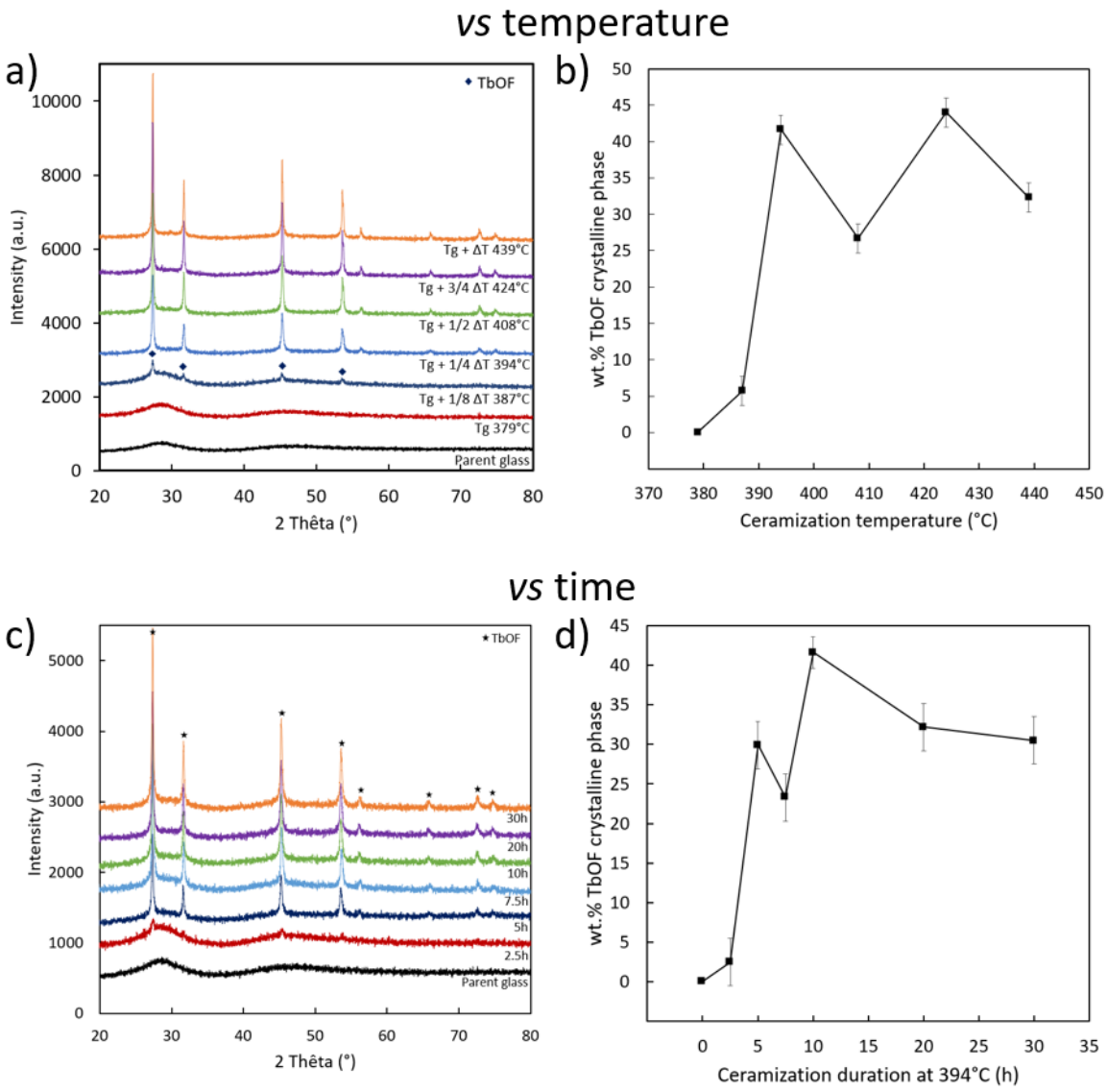

Figure 4.a) X-ray powder diffractograms of as-prepared glass-ceramics at different temperature of heat treatment for 10 hours. **b)** Crystalline fraction extracted from X-ray diffractograms in function of the ceramization temperature. **c)** X-ray diffractograms of as-prepared glass-ceramics at different time of heat treatment at 394°C. **d)** Crystalline fraction extracted from X-ray diffractograms in function of time of ceramization.

Optical analysis

UV-visible spectra were recorded from 200 to 800 nm on samples of 2mm thickness. Figure 5.a shows the transmission curves for different ceramization temperatures from room temperature up to 439°C. A variation of transmission at short wavelength which is attributed to the Rayleigh scattering is observed ; it increases with the ceramization temperature. Same spectra were recorded in function of time of ceramization from 0 to 30 hours at 394°C (figure 5.b). The Rayleigh scattering at short wavelength increases with the ceramization time to a plateau from 10 hours of heat treatment. These constant transmission properties from 10 hours are in good agreement with DSC and XRD. However, for temperature dependence, from DSC and XRD, a plateau of crystalline fraction and vitreous transition temperature is observed from 394°C but not for the transmission properties. To understand this observation, a morphological study was initiated.

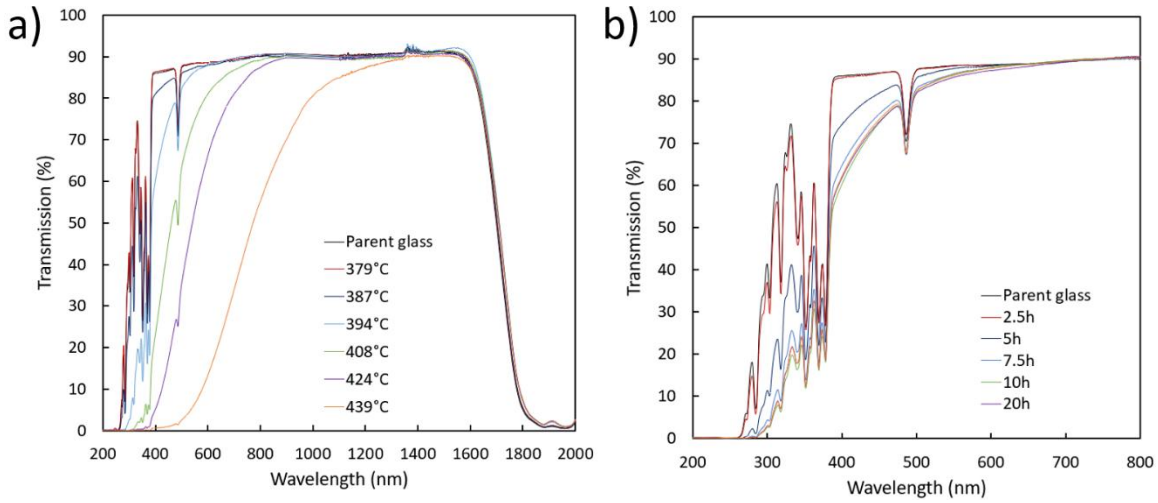

Figure 5. UV-Visible-NIR transmission spectra from 200 to 800 nm of sample of 2mm of thickness **a)** in function of the temperature for 10 hours of ceramization. **b)** in function of duration of ceramization at 394°C.

Morphological analysis

Scanning electron microscopy imaging of fragment of glass-ceramics obtained from different heat treatments are shown figure 6.a. Back-scattering electron imaging mode was used to highlight the chemical contrast to identify the crystalline particles formed. Crystallites appear in bright contrast due to their heavy elemental composition and confirm the potential of a terbium fluoride based crystalline phase. From room temperature to 379°C, homogeneous and amorphous samples are observed. However, from 387°C, the formation of a crystalline phase occurs with an increasing average size up to 439°C. The formation of larger particles from 408°C suggests an aggregation phenomenon relative to the temperature applied. This aggregate formation is in good

agreement with the constant crystalline fraction report in figure 4.b and the increasing of particle size.

From these electron microscopy images, 200 particles were measured at each temperature, to illustrate the size distribution and to follow more precisely the growth and sintering steps. Monodispersed populations following a normal distribution with an average population increasing from 41 ±4 to 173 ±41 nm of diameter are reported in figure 6.b. A broadening of the population is also observable with the increasing of the ceramization temperature; varying from 8 to 41 nm of standard deviation from 387 to 439°C. It can be directly related to the aggregation phenomenon; indeed, a larger and varying global size is measured due to the presence of non sintered and sintered particles. To highlight this sintering phenomenon, average size and standard deviation are reported in figure 6.c. Two different behaviours are observed, the first one between 387 and 394°C which is attributed to the growth phenomenon and a second one evolving linearly from 394 to 439°C which is related to the sintering process. The demonstration of this phenomenon is in agreement with the evolution observed by UV-Visible transmission measurements. Indeed, DSC and XRD show that no more crystalline phase is produced above 394°C but an increase of the Rayleigh scattering is observed. Rayleigh scattering is directly linked to the size of the particles in the material, in our case with the same crystalline phase obtained independently of the ceramization temperature. As the coalescence behavior increases, the size of the particles for a same crystalline fraction, the Rayleigh scattering increases too and induces a diminution of transmission at short wavelength. Crystallite size of TbOF extracted from XRPD show that the size evolution is comparable to particle size extracted from SEM pictures (supplementary information).

From 0 to 394°C, the crystallite size increases strongly from 0 to 46 ±6 nm. Then a linear slight increase of crystallite size is also observed between 394 and 439°C with values varying from 46 ±6 to 82 ±7 nm. It confirms the coalescence phenomenon. However, it appears that the particle diameter measured from SEM imaging corresponds to about two sintered TbOF crystallites.

The influence of the time of heat treatment on the size of nano crystallite formed is also observed via SEM. The obtained patterns are reported in figure 6.e for a ceramization duration varying from 0 to 30 hours at a fixed temperature of 394°C. As for the temperature study, patterns were recorded via back scattering electron to highlight nanometer size crystallites via the composition variation of the glass-ceramics between amorphous and crystalline phase The start of crystallization is observed after 2.5 hours of heat treatment. Then an evident increase of size between 2.5 and 10 hours is observed, related to the growing step of the crystalline phase. The patterns between 10 and 30 hours of ceramization appear to be quite similar.

From SEM images, a population distribution study was performed on 200 particles for each heat treatment duration. It shows a monodispersed population with an average size from 40 to 90 nm of diameter. Figure 6.f. shows the distribution function extracted from SEM imaging for different ceramization times. An increase of the average size is observed from 2.5 to 10 hours, then a constant value is maintained for ceramization durations over 10 hours. Also, a broadening of the population distribution is observed between 2.5 and 10 hours. The evolution of the average diameter and the standard deviation as a function of ceramization time is reported in figure 6.g. A sharp increase of the average size between 2.5 to 10 hours from 40 to 90 nm of diameter is observed, then a

constant value of 90 nm is obtained from 10 to 30 hours. In parallel, the standard deviation evolution shows a similar behavior with a sharp increase to 10 hours and a constant value around 15 nm between 10 and 30 hours. From these evolutions, two different behaviors are extracted. From 2.5 to 10 hours, the average size increase is attributed to crystal growth. For heat treatments over 10 hours, no variation of size or standard deviation can be observed, demonstrating the stability of the elaborated glass-ceramics. It shows that for ceramization durations longer than 10 hours, no morphological change occurs. The crystallite size of TbOF phase calculated from XRPD and Rietveld refinement in fucntion of ceramization duration exhibits a strong crystallization process between 0 and 10 hours with a crystallite size evolution from 0 to 46 ±6nm. Above 10 hours of ceramization no evolution is detected with values varying from 46 ±6 to 53 ±7nm. It is in good agreement with the SEM study after 10 hours of ceramization. Similarly, to the temperature evolution study, the particle size measured from SEM imaging appears to be twice the size of TbOF crystallites.

From DSC, XRD, absorption spectroscopy and SEM measurements, optimized synthesis parameters for maximal crystalline fraction and maximal transmission were determined. Indeed, the influence of Tb-based crystals formation in glass-ceramics on Faraday effect requires a maximal crystalline fraction to clearly identify the crystals influence and a maximal transmission to reach enough sensitivity for Verdet constant measurement. In function of temperature, each characterization shows a constant evolution of properties up to 394°C, at which temperature the integrated area of the first peak of crystallization reaches zero, the vitreous transition temperature is 416°C, and the crystalline fraction of

the cubic fluoride phase reaches 42 wt.%. Only TEM and SEM show strong variation between 394°C and 439°C due to the sintering process, i.e. an increase of the particles size by formation of "cauliflower like" agglomerate of sintered particles. As for Faraday effect, the transmission quality is an essential point, the more adapted temperature of heat treatment appears to be 394°C. The crystallization study as a function of ceramization time shows a constant evolution from 10 hours with an integrated area of the first crystallization peak close to zero, a vitreous transition around 403°C, and a crystalline fraction of the same cubic fluoride phase of 42 wt.%. In function of time, no variation of transmission or average size and standard deviation is observed between 10 and 30 hours. Thus, this crystallization study shows the possibility to control the crystallization process in our glass-ceramic samples. Compiled data show optimized crystallization parameters for the study of Faraday effect on glass-ceramics with a ceramization temperature of 394°C for 10 hours. Indeed, with these parameters, the crystalline fraction is maximal at 42 ±2 wt.% with cubic fluoride phase TbOF, the transmission properties show a nonimpact over 600 nm in comparison with parent glasses. The impact on transmission at shorter wavelength that 600 nm is relatively acceptable due to the good control of particle size, therefore of the Rayleigh scattering. The crystallization process is well controlled with the study on praseodymium-free samples. However, the substitution of terbium by praseodymium at different level without any influence on final properties of glass-ceramics further needs to be confirmed.

vs temperature

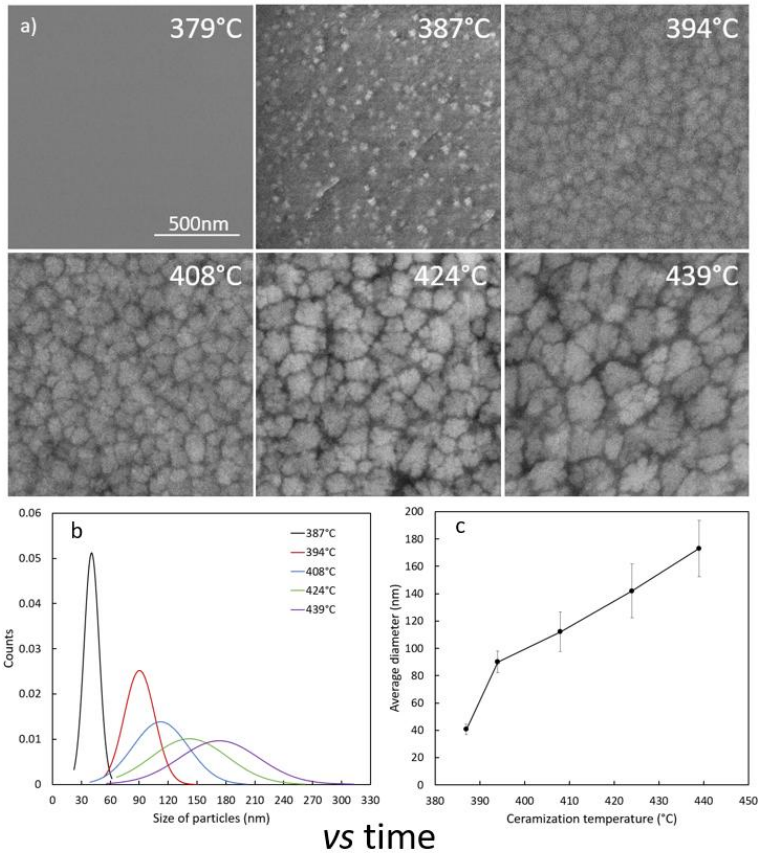

vs time

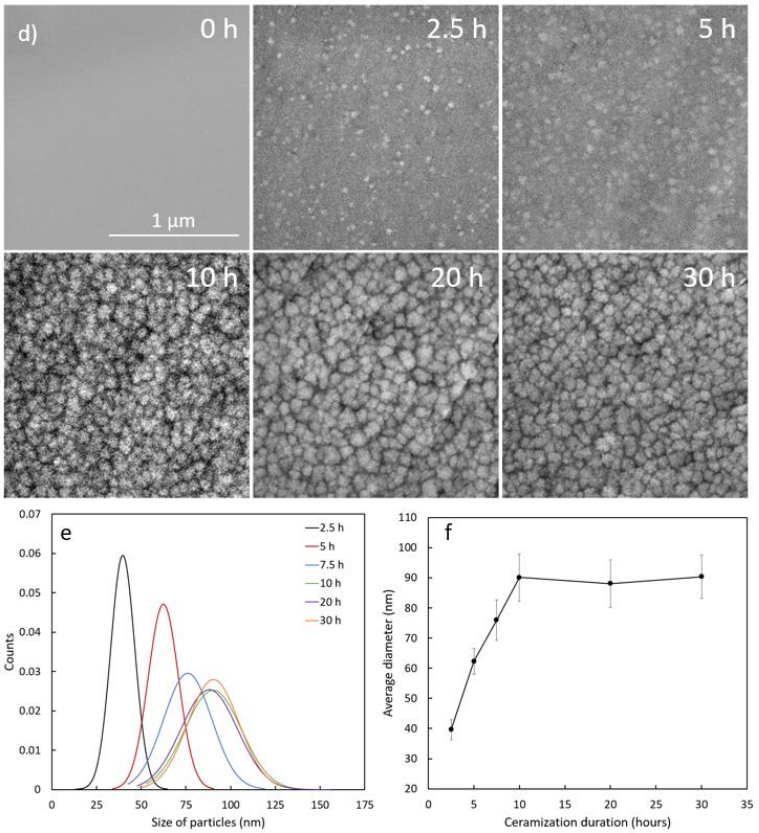

Figure 6.a) Scanning electron microscopy (back scattering electron mode) of Tb-Pr 0% samples heat-treated from 379°C to 439°C for 10 hours. **b)** Size distribution at different ceramization temperature and **c)** average particle size. **d)** Scanning electron microscopy of Tb-Pr 0% samples heat-treated at 394°C between 0 and 30 hours. **e)** Size distribution for different ceramization durations and **f)** average particle size.

Section 2: Co-doped glass-ceramics with varying co-dopant content.

Glass-ceramic samples were elaborated with a ceramization treatment at 394°C for 10 hours from parent glasses of composition 35 $NaPO_3$ - 15 BaF_2 – 0.5 (100 TbF_3 – x PrF_3) with x varying from 0 to 5, and are labelled Tb-Pr x%. DSC, XRD and SEM measurements were first performed to validate that praseodymium for terbium substitution in the glass does not influence the crystallization process. Then, Faraday measurements were realised on rods of 2 cm length and 4 mm diameter of glass-ceramic samples.

Control of crystallization in 35 $NaPO_3$ - 15 BaF_2 – 0.5 (100 TbF_3 – x PrF_3) glass-ceramics samples

To confirm the control of the crystallization process, DSC, XRD and SEM measurements were performed on prepared Tb-Pr glass-ceramic samples and compared to the optimal praseodymium-free glass-ceramic determined on section 1. Table 1 summarizes all the parameters extracted and used during the crystallization process study. Complementary DSC, XRD and SEM images are available in the Supplementary Information section to

lighten the manuscript. The glass transition temperatures for each sample are around 400°C. They reflect the same composition variation of vitreous phase in function of the crystallization independently to the praseodymium content. Similarly to results presented in section 1, a cubic fluoride phase TbOF (space group $Fm\bar{3}m$) is observed on XRD diffractograms. The cell-parameters increase with the increase of the terbium substitution rate by praseodymium. The atomic radii associated to Tb^{3+} and Pr^{3+} are 175 pm and 185 pm respectively. The terbium substitution by praseodymium induces an increase of the cell-parameters due to the variation of the ionic radius, in good agreement with the incorporation of praseodymium in the TbOF crystallites. To confirm the control of the size of the particles formed, SEM imaging and data processing from 200 particles measured were also used. The average size is homogeneous, around 90 nm of diameter, with the standard deviation varying gently between 11 and 18 nm. From these observations, it appears that the control and repeatability of the crystallization process is confirmed. Also, the substitution of terbium by praseodymium below 5 at.% does not have any influence on the crystallization process. At this point, the only difference between these glass-ceramic samples is the praseodymium content for a constant rare-earth concentration.

Table 1. Glass transition temperature, crystalline phase, average diameter, and standard deviation values extracted from DSC, XRD, and SEM measurement on Tb-Pr x% glass-ceramic samples heat-treated at 394°C for 10 hours.

Sample	Vitreous transition temperature (±2°C)	Crystalline phase	Average diameter	Standard deviation

			(nm)	(nm)
Tb-Pr 0%	402	Cubic $Fm\bar{3}m$	90	16
Tb-Pr 1%	400	Cubic $Fm\bar{3}m$	90	11
Tb-Pr 2%	402	Cubic $Fm\bar{3}m$	87	15
Tb-Pr 3%	400	Cubic $Fm\bar{3}m$	91	18
Tb-Pr 4%	399	Cubic $Fm\bar{3}m$	89	14
Tb-Pr 5%	398	Cubic $Fm\bar{3}m$	89	15

Faraday Effect

The Verdet constant measured at 600 nm for glass and glass-ceramic samples as a function of the praseodymium substitution rate is reported in figure 7.a. For the glass series, the Verdet constant increases from -81.9 to -84.2 rad.T^{-1}.m^{-1} at 600 nm for 0 and 1 at.% of terbium substitution by praseodymium, respectively. The highest Verdet constant value is obtained at both Tb-Pr 1% and Tb-Pr 2% glass samples. Above 2 at.%, the Verdet constant decreases to a minimal value of -78.7 rad.T^{-1}.m^{-1} for Tb-Pr 5%. Regarding glass-ceramics, the Verdet constant increases from 0 to 2 at.% with respective values of -80.8 to -84.7 rad.T^{-1}.m^{-1}. A slight decline of Verdet constant is measured from 2 to 4 at.% and a sharp decrease is observed to -82.7 rad.T^{-1}.m^{-1} for Tb-Pr 5%. A normalization of the Verdet constant by the total ionic density of lanthanide is required to

take into account all the influence parameters on the Faraday Effect such as sample thickness, magnetic field, wavelength, ionic density, and temperature. The Verdet constant is taking into account the sample thickness and the magnetic field. The measurements were realized at 293 K and values are compared at the same wavelength. The ionic density is calculated using the following equation.

$$N_{RE\ total} = \sum_{RE} \frac{\rho\ wt.\%(RE)\ Na}{M(RE)}$$

The terbium fraction used for glass-ceramic samples is the same than for glass samples because the heat treatment triggering crystallization does not induce any macroscale variation of composition. The density values for glass and glass-ceramics are shown in figure 7.b. A quasi-linear evolution is observed for both series, in good agreement with the weight and ionic radius variation between terbium and praseodymium. The density of glass-ceramics is higher than for the glass samples with a variation from 5.136 ±0.010 to 5.103 ±0.009 $g.cm^{-3}$ from Tb-Pr 0% and Tb-Pr 5%. The glass sample density varies from 5.097 ±0.006 to 5.070 ±0.009 $g.cm^{-3}$ between Tb-Pr 0% and Tb-Pr 5%. From these density values, the total ionic density of lanthanide is calculated for each sample and the Verdet constant at 600 nm normalized by ionic density is reported in figure 7.c. Firstly, a very similar behavior is observed for both series. Initial normalized Verdet constant for praseodymium-free samples is different with values of $-8.23.10^{21}$ and $-8.02.10^{21}$ $rad.T^{-1}.m^{-1}.ions^{-1}$ for Tb-Pr 0% glass and glass-ceramic, respectively. This variation is related to the change of direct environment and geometry of terbium ions between glass and glass-ceramics. Indeed, in glass ceramics, the terbium is observed in the amorphous geometry specific to glass matrix and the crystalline geometry from the TbOF crystallites. The

geometry and the nature of next neighbor cation have influence on the Verdet constant and can explain the variation of the initial Verdet constant measured in the praseodymium-free sample in both glass and glass-ceramic cases. This environment influence is also observed for example in the case of $Tb_3Ga_5O_{12}$ [4] and $Tb_3Al_5O_{12}$ [31] garnet single crystals exhibiting respective Verdet constants of -134 and -174 $rad.T^{-1}.m^{-1}$ at 632 nm and densities of 7.13 and 6.06 $g.cm^{-3}$. The normalization of the Verdet constant by the ionic density for these single crystals of same crystalline structure gives values of $-1.06.10^{20}$ and $-1.28.10^{20}$ $rad.T^{-1}.m^{-1}.ions^{-1}$ for TGG and TAG, respectively. The superexchange interaction between the terbium ions and other cations from the matrix is not negligible [32]. The glass sample reaches a maximum at $-8.51.10^{21}$ $rad.T^{-1}.m^{-1}.ions^{-1}$ while a maximal value of $-8.62.10^{21}$ $rad.T^{-1}.m^{-1}.ions^{-1}$ is obtained for glass-ceramic samples in the case of Tb-Pr 2% in both series. This Verdet constant increase is attributed to the co-doping effect and directly to superexchange influence on Zeeman Effect at the origin of the Faraday rotation. To quantify this effect, the co-doping efficiency (CDE) is calculated using the following equation [19].

$$CDE = \frac{V_{d\ Tb-\mathrm{Pr}\ x\%}}{V_{d\ Tb-\mathrm{Pr}\ 0\%}}$$

The CDE variation in glass and glass-ceramic series calculated from normalized Verdet constant for different wavelength of measurements is reported in figure 7.d. Both series exhibit the same CDE shape of variation in function of the praseodymium rate of substitution. For the measurements performed at 600 nm, the maximal CDE obtained for glass and glass-ceramic samples is respectively 1.037 and 1.075. It represents an increase of 3.7 and 7.5% of Verdet constant compared to the praseodymium-free sample for the

same lanthanide concentration. This increase is attributed in the literature to the superexchange interaction between the terbium and praseodymium because all the other parameters of influence are taken into account and the only varying parameter is the substitution of terbium by praseodymium. The CDE variation at different measurement wavelengths show a stability of the phenomenon from visible to near infrared ranges.

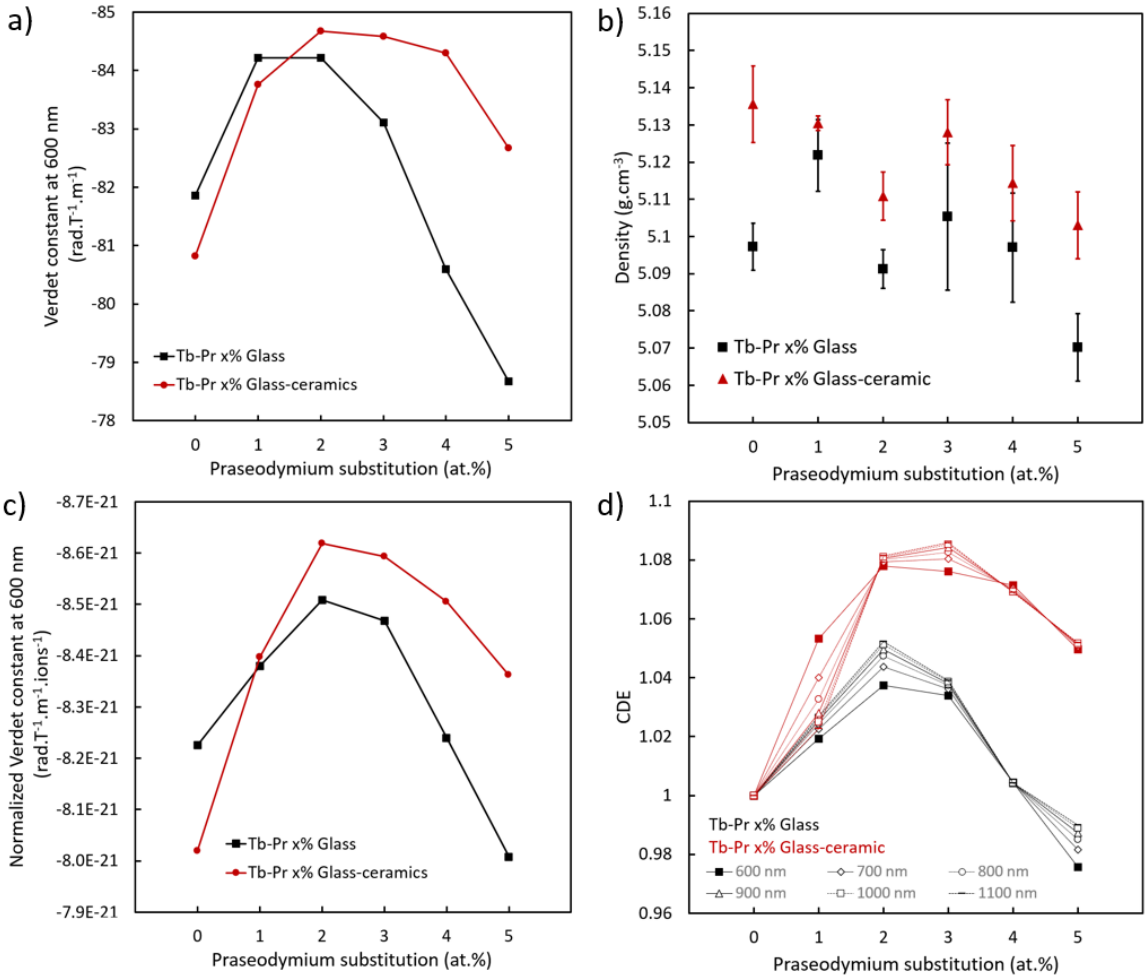

Figure 7.a) Verdet constant at 600 nm, b) densities, c) Normalized Verdet constant at 600 nm and d) CDE from 600 to 1100 nm as a function of the praseodymium substitution for terbium in at.% for glass and glass-ceramic samples.

In our previous work, the co-doping efficiency was lower in glass sample matrix compared to values calculated from TGG single crystal reported in the literature [4]. The variation of angle and bond length relative to superexchange interaction occurring in glass matrix compared to the crystal structure was the hypothesis to explain this observation [19]. The CDE increase compared to glass and glass-ceramics from identical composition seems to confirm this hypothesis. Indeed, the superexchange interaction in glass-ceramics is more efficient in a crystalline phase rather than in a glass phase due to the better orbital overlapping.

Based on this observation, from a defined composition with a high concentration in terbium ions, the controlled substitution with another lanthanide coupled to a precise crystallization control leads to an increasing up to 8% of the Verdet constant for the same total lanthanide concentration.

Conclusion

In summary, the crystallization process occurring in fluorophosphate glass of composition 35 $NaPO_3$ – 15 BaF_2 – 50 TbF_3 was explored. A precise control of the crystallisation parameters is possible and enable tailoring the final morphology of the crystallites. DSC, XRD, Transmission and SEM measurements showed that the crystalline phase corresponds to the TbOF cubic fluorite phase, most probably enriched in Ba, i.e. corresponding to $Tb_{1-x}Ba_xO_{1-x}F_{1+x}$. An optimal crystalline fraction of 42 ± 2 wt.% with an average crystallite size of 90 nm is obtained for a heat treatment of 10 hours at 394°C. In a second part, magneto-optical properties of glass-ceramics of composition

35 $NaPO_3$ – 15 BaF_2 – 0.5 ((100-x) TbF_3 – x PrF_3) with x = 0, 1, 2, 3, 4 and 5 were elaborated at the optimal heat treatment parameters defined in part one. The non-influence of the praseodymium substitution below 5 at.% on the crystallization process is reported. The Verdet constant of the glass-ceramics shows an identical behavior with the parent glasses. Indeed, the Verdet constant increases from -80.8 $rad.T^{-1}.m^{-1}$ for Tb-Pr 0% to reach a maximum of -84.7 $rad.T^{-1}.m^{-1}$ for Tb-Pr 2%. However, the crystalline environment of the lanthanide cation sites optimizes the co-doping influence with an increase of 8% in the case of glass-ceramics which is twice higher than for glass samples and their amorphous geometry. This effect permits to increase significantly the Verdet constant of materials with the same total lanthanide concentration. This observation has both benefits on the knowledge about the superexchange interaction influence on Faraday effect and its mechanism and to extend the limits of achievable Verdet constants for a fixed concentration.

Acknowledgement

This project has benefited from the facilities of the Platform MACLE-CVL which was co-funded by the European Union and Centre-Val de Loire Region (FEDER).

Bibliography

(1) Vojna, D.; Slezák, O.; Lucianetti, A.; Mocek, T. Verdet Constant of Magneto-Active Materials Developed for High-Power Faraday Devices. *Appl. Sci.* **2019**, *9* (15), 3160. https://doi.org/10.3390/app9153160.
(2) Kawashima, A.; Nakanishi, T.; Kitagawa, Y.; Fujita, K.; Tanaka, K.; Fushimi, K.; Malik, M. A.; O'Brien, P.; Hasegawa, Y. Terbium Oxide, Fluoride, and Oxyfluoride Nanoparticles with Magneto-Optical Properties. *Bull. Chem. Soc. Jpn.* **2015**, *88* (10), 1453–1458. https://doi.org/10.1246/bcsj.20150198.

(3) Gao, G.; Winterstein-Beckmann, A.; Surzhenko, O.; Dubs, C.; Dellith, J.; Schmidt, M. A.; Wondraczek, L. Faraday Rotation and Photoluminescence in Heavily Tb3+-Doped GeO2-B2O3-Al2O3-Ga2O3 Glasses for Fiber-Integrated Magneto-Optics. *Sci. Rep.* **2015**, *5* (1), 8942. https://doi.org/10.1038/srep08942.
(4) Raja, M. Y. A.; Allen, D.; Sisk, W. Room- temperature Inverse Faraday Effect in Terbium Gallium Garnet. *Appl. Phys. Lett.* **1995**, *67* (15), 2123–2125. https://doi.org/10.1063/1.114740.
(5) Ding, J.; Man, P.; Chen, Q.; Guo, L.; Hu, X.; Xiao, Y.; Su, L.; Wu, A.; Zhou, Y.; Zeng, F. Influence of Tb 3+ Concentration on the Optical Properties and Verdet Constant of Magneto-Optic ABS-PZZ Glass. *Opt. Mater.* **2017**, *69*, 202–206. https://doi.org/10.1016/j.optmat.2017.04.036.
(6) Letellier, V.; Seignac, A.; Le Floch, A.; Matecki, M. Magneto-Optical Properties of Heavily Rare-Earth Doped Non-Crystalline Fluorophosphates. *J. Non-Cryst. Solids* **1989**, *111* (1), 55–62. https://doi.org/10.1016/0022-3093(89)90423-7.
(7) Guo, H.; Wang, Y.; Gong, Y.; Yin, H.; Mo, Z.; Tang, Y.; Chi, L. Optical Band Gap and Photoluminescence in Heavily Tb 3+ Doped GeO 2 -B 2 O 3 -SiO 2 -Ga 2 O 3 Magneto-Optical Glasses. *J. Alloys Compd.* **2016**, *686*, 635–640. https://doi.org/10.1016/j.jallcom.2016.06.074.
(8) Jia, H.; Zhu, Z. Concentration-Wavelength Dependence of Magneto-Optical Properties in Tb3+-Doped BGAP Glass. *J. Non-Cryst. Solids* **2021**, *552*, 120456. https://doi.org/10.1016/j.jnoncrysol.2020.120456.
(9) Zhou, L.; Zhu, Z. Magneto-Optical and Luminescent Properties of Tb3+ Ions Doped GBPZ Magneto-Optical Glass. *J. Non-Cryst. Solids* **2021**, *574*, 121165. https://doi.org/10.1016/j.jnoncrysol.2021.121165.
(10) Yang, H.; Zhu, Z. Magneto-Optical Glass Mixed with Tb3+ Ions: High Verdet Constant and Luminescence Properties. *J. Lumin.* **2021**, *231*, 117804. https://doi.org/10.1016/j.jlumin.2020.117804.
(11) Bellanger, B.; Ledemi, Y.; Messaddeq, Y. Fluorophosphate Glasses with High Terbium Content for Magneto-Optical Applications. *J. Phys. Chem. C* **2020**, *124* (9), 5353–5362. https://doi.org/10.1021/acs.jpcc.9b11696.
(12) Wang, X.; Yang, L.; Chen, Z.; Wang, J.; Hong, J.; Wang, Y.; Shi, C.; Zhang, P.; Zhang, L.; Hang, Y. Growth and Faraday Rotation Characteristics of Tb3−xNdxGa5O12 Single Crystal. *Opt. Mater.* **2015**, *47*, 157–160. https://doi.org/10.1016/j.optmat.2015.04.044.
(13) Chen, Z.; Yang, L.; Wang, X.; Wang, J.; Hang, Y. Fabrication and Characterizations of a Erbium Doped Terbium Gallium Garnet Crystal for Faraday Rotators. *Mater. Lett.* **2015**, *161*, 93–95. https://doi.org/10.1016/j.matlet.2015.08.085.
(14) Chen, Z.; Yang, L.; Hang, Y.; Wang, X. Improving Characteristic of Faraday Effect Based on the Tm 3+ Doped Terbium Gallium Garnet Single Crystal. *J. Alloys Compd.* **2016**, *661*, 62–65. https://doi.org/10.1016/j.jallcom.2015.11.162.
(15) Chen, Z.; Yang, L.; Hang, Y.; Wang, X. Faraday Effect Improvement by Dy3+-Doping of Terbium Gallium Garnet Single Crystal. *J. Solid State Chem.* **2016**, *233*, 277–281. https://doi.org/10.1016/j.jssc.2015.10.041.
(16) Chen, Z.; Hang, Y.; Yang, L.; Wang, J.; Wang, X.; Hong, J.; Zhang, P.; Shi, C.; Wang, Y. Fabrication and Characterization of Cerium-Doped Terbium Gallium

Garnet with High Magneto-Optical Properties. *Opt. Lett.* **2015**, *40* (5), 820. https://doi.org/10.1364/OL.40.000820.
(17) Chen, Z.; Hang, Y.; Yang, L.; Wang, J.; Wang, X.; Zhang, P.; Hong, J.; Shi, C.; Wang, Y. Great Enhancement of Faraday Effect by Pr Doping Terbium Gallium Garnet, a Highly Transparent VI-IR Faraday Rotator. *Mater. Lett.* **2015**, *145*, 171–173. https://doi.org/10.1016/j.matlet.2015.01.108.
(18) Chen, Z.; Yang, L.; Wang, X.; Yin, H. High Magneto-Optical Characteristics of Holmium-Doped Terbium Gallium Garnet Crystal. *Opt. Lett.* **2016**, *41* (11), 2580. https://doi.org/10.1364/OL.41.002580.
(19) Bellanger, B.; Audebert, L.; Ledemi, Y.; Messaddeq, Y. Superexchange Interaction Influence on the Faraday Effect in Terbium Fluorophosphate Glasses by Co-Doping with Praseodymium, Dysprosium, and Holmium. *J. Phys. Chem. C* **2021**, *125* (31), 17482–17492. https://doi.org/10.1021/acs.jpcc.1c04713.
(20) Ledemi, Y.; Trudel, A.-A.; Rivera, V. A. G.; Chenu, S.; Véron, E.; Nunes, L. A.; Allix, M.; Messaddeq, Y. White Light and Multicolor Emission Tuning in Triply Doped Yb^{3+} /Tm^{3+} /Er^{3+} Novel Fluoro-Phosphate Transparent Glass-Ceramics. *J Mater Chem C* **2014**, *2* (25), 5046–5056. https://doi.org/10.1039/C4TC00455H.
(21) Rahimian, H.; Hatefi, Y.; Dehghan Hamedan, A.; Shirmardi, S. P.; Mokhtari, H. Structural and Optical Investigations on Eu3+ Doped Fluorophosphate Glass and Nano Glass-Ceramics. *J. Non-Cryst. Solids* **2018**, *487*, 46–52. https://doi.org/10.1016/j.jnoncrysol.2018.02.017.
(22) de Queiroz, T. B.; Botelho, M. B. S.; Gonçalves, T. S.; Dousti, M. R.; de Camargo, A. S. S. New Fluorophosphate Glasses Co-Doped with Eu3+ and Tb3+ as Candidates for Generating Tunable Visible Light. *J. Alloys Compd.* **2015**, *647*, 315–321. https://doi.org/10.1016/j.jallcom.2015.06.066.
(23) Hu, Z.; Wang, Y.; Ma, E.; Chen, D.; Bao, F. Microstructures and Upconversion Luminescence of Er3+ Doped and Er3+/Yb3+ Co-Doped Oxyfluoride Glass Ceramics. *Mater. Chem. Phys.* **2007**, *101* (1), 234–237. https://doi.org/10.1016/j.matchemphys.2006.04.001.
(24) Wei, Y.; Li, J.; Yang, J.; Chi, X.; Guo, H. Enhanced Green Upconversion in Tb3+–Yb3+ Co-Doped Oxyfluoride Glass Ceramics Containing LaF3 Nanocrystals. *J. Lumin.* **2013**, *137*, 70–72. https://doi.org/10.1016/j.jlumin.2012.11.017.
(25) Chen, Q. J.; Zhang, W. J.; Huang, X. Y.; Dong, G. P.; Peng, M. Y.; Zhang, Q. Y. Efficient Down- and up-Conversion of Pr3+–Yb3+ Co-Doped Transparent Oxyfluoride Glass Ceramics. *J. Alloys Compd.* **2012**, *513*, 139–144. https://doi.org/10.1016/j.jallcom.2011.10.007.
(26) Wang, R.; Zhou, D.; Qiu, J.; Yang, Y.; Wang, C. Color-Tunable Luminescence in Eu3+/Tb3+ Co-Doped Oxyfluoride Glass and Transparent Glass–Ceramics. *J. Alloys Compd.* **2015**, *629*, 310–314. https://doi.org/10.1016/j.jallcom.2014.12.233.
(27) De La Torre, A. G.; Bruque, S.; Aranda, M. A. G. Rietveld Quantitative Amorphous Content Analysis. *J. Appl. Crystallogr.* **2001**, *34* (2), 196–202. https://doi.org/10.1107/S0021889801002485.
(28) Orlhac, X.; Fillet, C.; Deniard, P.; Dulac, A. M.; Brec, R. Determination of the Crystallized Fractions of a Largely Amorphous Multiphase Material by the Rietveld Method. *J. Appl. Crystallogr.* **2001**, *34* (2), 114–118. https://doi.org/10.1107/S0021889800017908.

(29) Brindley, G. W. XLV. The Effect of Grain or Particle Size on x-Ray Reflections from Mixed Powders and Alloys, Considered in Relation to the Quantitative Determination of Crystalline Substances by x-Ray Methods. *Lond. Edinb. Dublin Philos. Mag. J. Sci.* **1945**, *36* (256), 347–369. https://doi.org/10.1080/14786444508520918.
(30) Cheary, R. W.; Coelho, A. A.; Cline, J. P. Fundamental Parameters Line Profile Fitting in Laboratory Diffractometers. *J. Res. Natl. Inst. Stand. Technol.* **2004**, *109* (1), 1. https://doi.org/10.6028/jres.109.002.
(31) Geho, M.; Sekijima, T.; Fujii, T. Growth of Terbium Aluminum Garnet (Tb3Al5O12; TAG) Single Crystals by the Hybrid Laser Floating Zone Machine. *J. Cryst. Growth* **2004**, *267* (1–2), 188–193. https://doi.org/10.1016/j.jcrysgro.2004.03.068.
(32) Xu, Y.; Zhang, G.; Duan, M. Calculations of the Faraday Rotation in RE- substituted Iron Garnets. *J. Appl. Phys.* **1993**, *73* (10), 6133–6135. https://doi.org/10.1063/1.352725.